

Article

# Petrology of Peridotites and Nd-Sr Isotopic Composition of Their Clinopyroxenes from the Middle Andaman Ophiolite, India

Tomoaki Morishita <sup>1,2,\*</sup>, Masako Yoshikawa <sup>3</sup>, Akihiro Tamura <sup>1</sup>, Juan Miguel Guotana <sup>4</sup> and Biswajit Ghosh <sup>1,5</sup>

<sup>1</sup> Faculty of Geosciences and Civil Engineering, Institute of Science and Engineering, Kanazawa University, Kanazawa 920-1192, Japan; aking826@gmail.com (A.T.); bghosh\_geol@hotmail.com (B.G.)

<sup>2</sup> Lamont-Doherty Earth Observatory, Columbia University, Palisades, NY 10964, USA

<sup>3</sup> Department of Earth and Planetary Systems Science, Graduate School of Science, Hiroshima University, 1-3-2 Kagamiyama, Higashi-Hiroshima City, Hiroshima 739-8511, Japan; masako@hiroshima-u.ac.jp

<sup>4</sup> Graduate School of Natural Science & Technology, Kanazawa University, Kanazawa 920-1192, Japan; jmguotana@stu.kanazawa-u.ac.jp

<sup>5</sup> Department of Geology, University of Calcutta, 35 Ballygunge Circular Road, Kolkata 700 019, India

\* Correspondence: tomo\_make\_a\_wish@icloud.com; Tel.: +81-76-264-6513

Received: 26 May 2018; Accepted: 13 September 2018; Published: 17 September 2018



**Abstract:** The Andaman Ophiolite, India, is located at the southeastern end of the Tethyan ophiolites. We examine petrology and mineralogy of two lherzolites and a completely serpentinized dunite associated with lherzolite from the middle Andaman Island. Major and trace element compositions of minerals in the lherzolites suggest their residual origin after low-degree of partial melting with less flux infiltration, and are similar to those of abyssal peridotites recovered from mid-ocean ridges. The dunite with spinels having low-Cr/(Cr + Al) ratio was formed by interaction between peridotite and mid-ocean ridge basalt-like melt. The <sup>87</sup>Sr/<sup>86</sup>Sr and <sup>143</sup>Nd/<sup>144</sup>Nd isotopic systematics of clinopyroxenes of the two lherzolites are consistent with MORB-type mantle source. Petrology and light rare earth element (LREE)-depleted patterns of clinopyroxene from the studied lherzolites are the same as those from some of the western Tethyan ophiolites. The age-corrected initial  $\epsilon$ Nd values of the Tethyan lherzolite clinopyroxenes with LREE-depleted patterns are likely to be consistent with the depleted mantle evolution line.

**Keywords:** the Andaman ophiolite; peridotite; Nd-Sr isotopes

## 1. Introduction

The Mesozoic peri-Gondwanan ophiolites are distributed in the Alpine-Himalayan orogenic belt, the Indo-Myanmar (Burma) Range and the Sunda subduction zone [1–4]. These ophiolites were formed by the closing of the Tethyan oceans with different ages, such as the Paleo-Tethys (Devonian–Triassic), Meso-Tethys (late Early Permian–Late Cretaceous) and Neo-Tethys (Late Triassic–Late Cretaceous) [2]. Based on the abundances of dominant ultramafic rocks in the Tethyan ophiolites, two subtypes of peridotite bodies have been recognized: the lherzolite-subtype ultramafic bodies and the harzburgite-subtype ultramafic bodies e.g., [5]. Peridotite samples obtained from Western and Central Europe, such as the Alpine Tethys, the Pyrenian domain, the Dinarides and Hellenides, and the Ibra-Newfoundland rifted margins, were reviewed in petrology and mineralogy by Picazo et al. [6]. Some of the harzburgite-subtype bodies have been interpreted to be formed as residue after high degree of partial melting, enhanced by infiltration of subduction-induced fluids e.g., [7]. On the other hand, lherzolitic peridotites in the lherzolite-subtype bodies in these areas are akin to the present day

abyssal peridotites from mid-ocean ridges, and appears to be least modified by late subduction events. The lherzolite-dominated bodies in the Tethyan ophiolites will, therefore, provide an opportunity to explore the nature and variation of the Tethyan oceanic upper mantle.

A number of dismembered ophiolitic slices are exposed in the N–S trends all along the Andaman Islands and are referred to as the Andaman ophiolite [8–10]. The Andaman ophiolite is located in the southeast end of the Tethyan ophiolite belt. In terms of petrography and mineral chemistry of the ophiolitic rocks, especially peridotite bodies, there exists a pronounced variation between the Rutland Island in the south and middle/north Andaman [9,11,12]. The Rutland Island peridotites are mainly composed of harzburgite and high-Cr chromitite indicating their formation in supra-subduction zone environments, whereas lherzolite-dominated outcrops are well observed in the middle/north Andaman Island [4,8,9,12]. The Middle Andaman lherzolite is the southeastern end of the lherzolite-subtype Tethyan ophiolites.

We analyzed Sr and Nd isotopic compositions of clinopyroxene separates of two representative lherzolite samples from the middle Andaman ophiolite. The first order objective of this study was to characterize the Middle Andaman lherzolite and to address the key question concerning the nature of lherzolitic mantle domain of Tethyan ophiolite.

## 2. Middle Andaman Peridotites: Geological Background, Samples and Their Petrography

The Andaman Islands constitute the central part of the Burma-Sunda-Java subduction zone (Figure 1). The oceanic part of the Indian Plate is subducting towards the east below the Southeast Asian Plate at the western side of the Andaman Islands [13]. Sensitive high-resolution ion microprobe (SHRIMP) U-Pb isotope analyses of zircons from the granitic rocks in the Andaman Ophiolite assign an age >95 Ma [14,15] and 116–119 Ma [16], respectively. Most of these granitic rocks intrude into volcanic rocks/plutons of the Andaman ophiolite and have arc-related geochemical affinities [15–17]. The U-Pb zircon age of these granitic rocks may represent later arc stage magmatism in the Andaman Ophiolite [4].

The peridotites at Andaman and Rutland islands are generally serpentinized/weathered with variable degrees (40–80 vol.% in general) [4,9,12]. However, the primary mineralogy of the serpentinites is mostly preserved irrespective of serpentinization. Lherzolites with small amounts of dunitic/harzburgitic rocks are exposed along the coast line of the middle Andaman (Figure 2) whereas most of the land areas are covered with soil and thick vegetation. Lherzolitic samples are usually protogranular to porphyroclastic in textures (Figures 2 and 3), although highly foliated to mylonitic textures are sometimes observed in boulders (Figure 3). Pyroxenite and gabbro veins, a few millimeters to a few centimeters thick, rarely cut the host peridotites (Figure 3).

To avoid mineralogical and geochemical modifications caused by serpentinization, deformation and infiltration of late melts related to the formation of pyroxenite/gabbro veins, we selected two least serpentinized, less deformed and vein-free spinel lherzolites for further mineralogical and geochemical investigations: one from a massive outcrop of a quarry where no visible variations in terms of modal abundances of pyroxene were observed on the weathered surface (M21), and the other is one of the least altered/deformed clinopyroxene-rich lherzolite boulders (M31) recovered from the strand line (Figures 2 and 3). Both lherzolite samples are moderately serpentinized showing protogranular texture with 15 vol.% (M31) and 12 vol.% (M21) of modal clinopyroxene (Figure 4). Coarse-grained porphyroclastic clinopyroxene is observed in M31 (Figure 4). One dunite sample (M42DH), which is completely serpentinized, in a lherzolite host is also examined (Figure 3). The lithological boundary between dunites and the lherzolite host is sharp in terms of mineral mode variation. Chromian spinel in M42DH is mostly altered to magnetite, but the relict primary spinel remains with thick magnetite rim is still observed in coarser grains (Figure 5).

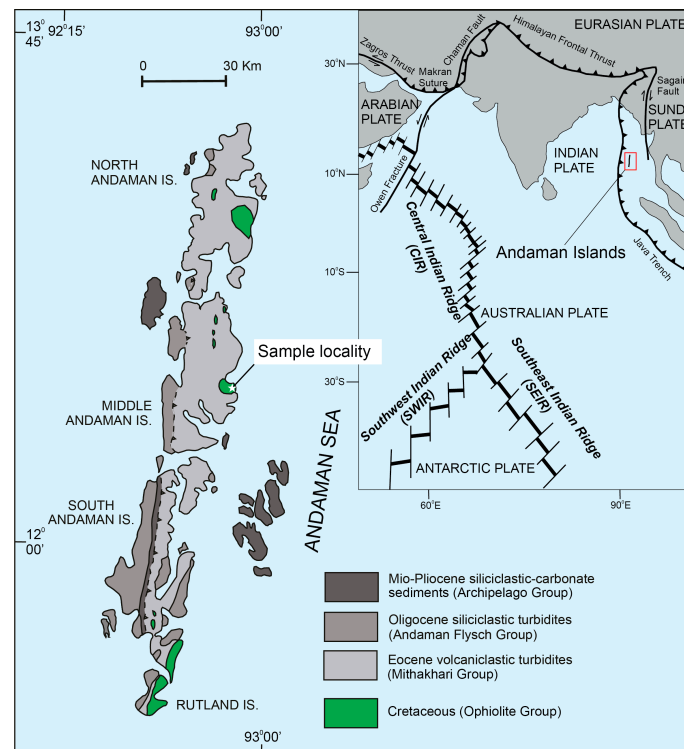


**Figure 1.** Geology of the Andaman Islands (simplified after [12] showing the sample localities from the Middle Andaman Ophiolites (green in color)).

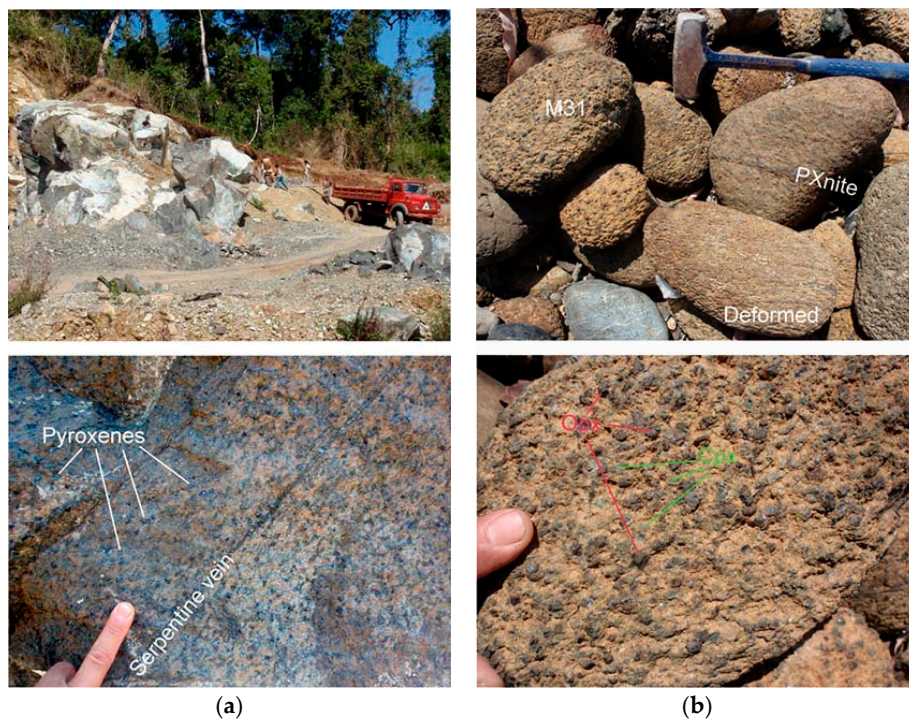


**Figure 2.** (a) Upper, massive lherzolite exposure in a quarry (location of M21). Lower, close-up of M21. (b) Upper, pyroxene-rich peridotite boulders along the coast. The studied M31. Lower, close-up of M31. Emerald green clinopyroxene (Cpx) and relatively dark orthopyroxene (Opx) are visible on weathered surface (b).

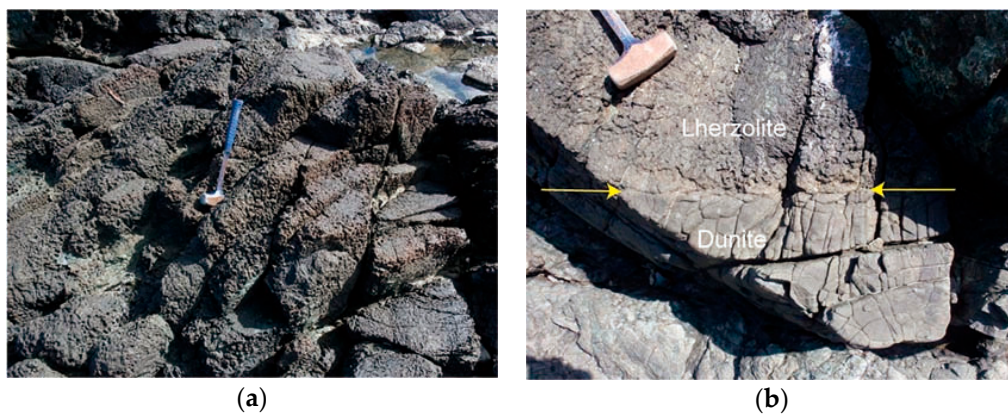


**Figure 3.** Dunite is easily distinguished from the host lherzolite (a) (rough surface because of pyroxene porphyroclasts) by smooth weathered surface, (b) indicating that mineral mode is abruptly changed from the host peridotite to the dunite pod (yellow arrows).

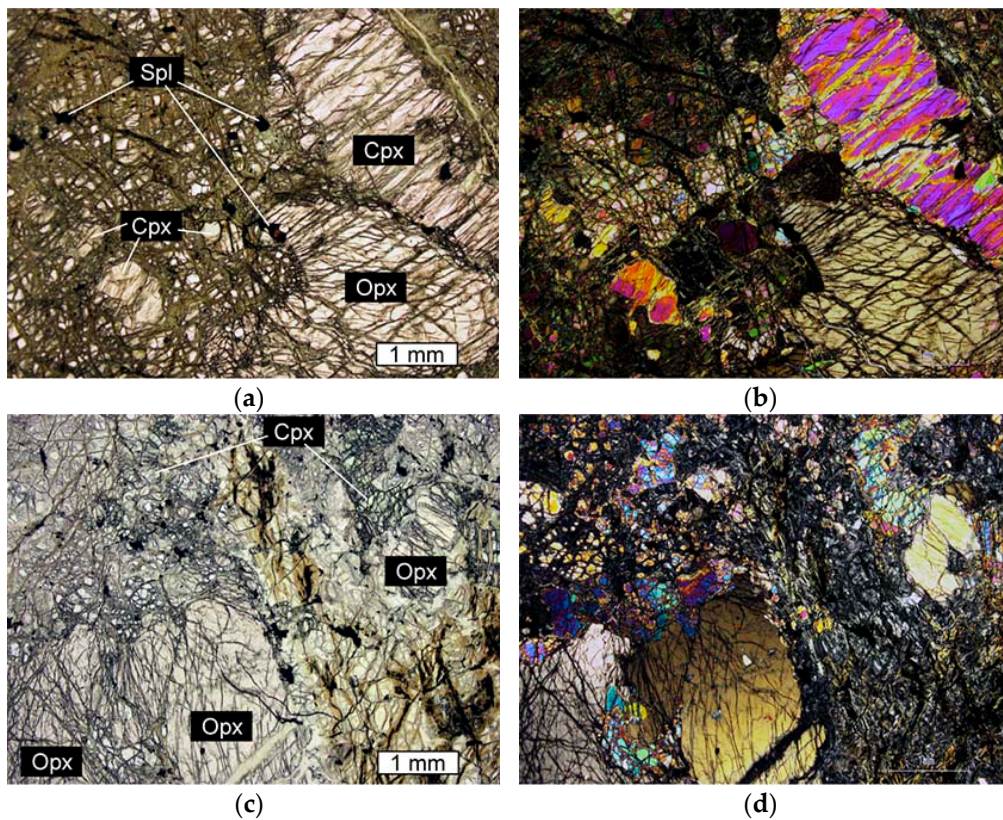


**Figure 4.** Photomicrograph of the studied lherzolite samples. (M31) (a) Plane-polarized light and (b) cross-polarized light images of M31. Coarse-grained clinopyroxene porphyroclast is observed. (c) Plane-polarized light and (d) cross polarized light images of M21. Cpx = clinopyroxene, Opx = orthopyroxene, Spl = spinel.

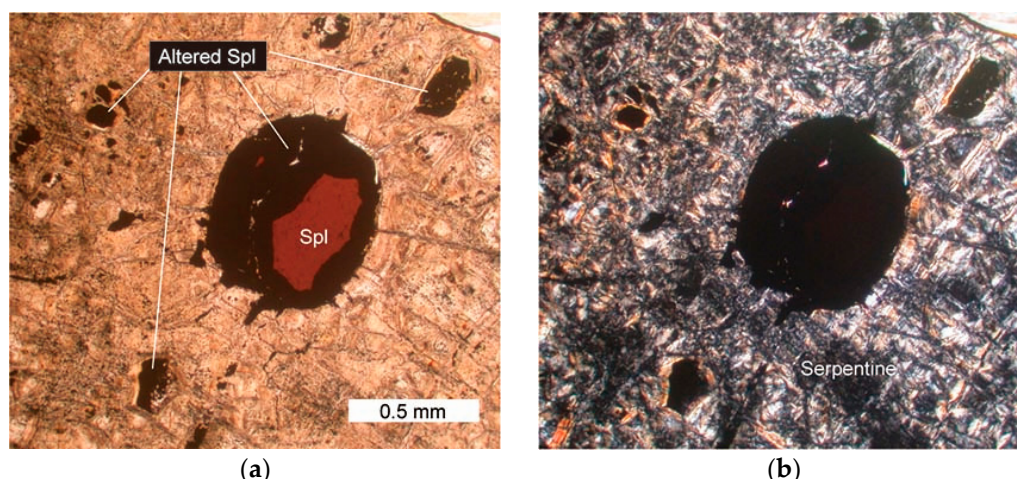


**Figure 5.** Photomicrograph of the dunite sample (M42DH). (a) Plane-polarized light. (b) Cross-polarized light. Reddish brown-colored primary spinel is observed in an altered spinel (Spl). Fully altered spinels, now magnetites, occur in totally serpentinized olivine matrix.

### 3. Analytical Methods

In this study, two lherzolite (M21 and M31) and one dunite (M42DH) samples have been used for geochemical analyses. Major-element compositions of minerals (Tables 1–3) are determined using an electron probe micro-analyzer (EPMA, JEOL JXA-8800 Superprobe) at Kanazawa University, Kanazawa, Japan. The analyses are performed under an accelerating voltage of 15 kV and a beam current of 20 nA, using a 3  $\mu\text{m}$  diameter beam. X-ray peaks were counted for 10s to 50 s, and both high and low backgrounds are measured. JEOL software (JEOL, Tokyo, Japan) using ZAF corrections was also employed. The following standards were used: quartz = Si;  $\text{KTiPO}_4$  = K and Ti; corundum = Al; eskolaite = Cr; fayalite = Fe; manganosite = Mn; periclase = Mg; wollastonite = Ca; jadeite = Na; and nickel oxide = Ni. In-house mineral standards (olivine, chromian spinel, diopside, and K-feldspar) are measured repeatedly to monitor data quality. The measured concentrations in these minerals are consistent with the averaged values from long-term analyses, within one standard deviation for every element. Data precision established through multiple analyses of one point in the house-prepared standard minerals is better than 5% and 10% relative standard deviation from the averaged values for elements with abundances of >0.5 wt.% and <0.5 wt.%, respectively. Rare earth element (REE) and trace element (Li, Ti, Sr, Y, Zr, Nb and Hf) compositions of their clinopyroxenes were already reported by [4]. Complete data sets of both major and trace element compositions of clinopyroxenes are shown in Table 3. Here we use trace element data [4] for further discussions.

For Sr and Nd isotopes, the samples are first thin sliced and lightly crushed. Clinopyroxenes are carefully handpicked under a binocular microscope to select fresh, uniform in color, fracture-free and inclusion-free pure grains. These clinopyroxenes are leached repeatedly following the methods of [18] to eliminate the effects of seawater alteration. The Sr and Nd isotopes of clinopyroxenes are measured by thermal-ionization mass spectrometry (TIMS) on a Thermo-Finnigan MAT 262 instrument at Beppu Geothermal Research Laboratory, Kyoto University, Japan. Details of the Sr-Nd isotope analyses can be found in [19,20]. Data are shown in Table 4.

**Table 1.** Representative compositions of olivine and orthopyroxene.

Sample		M21				
Mineral	Olivine Average	STD (N = 7)	OPX-3-core	OPX-3-rim	OPX-10-core	OPX-10-rim
SiO <sub>2</sub>	41.2	0.18	55.1	57.5	55.6	56.5
TiO <sub>2</sub>	<0.04		<0.04	<0.04	<0.04	<0.04
Al <sub>2</sub> O <sub>3</sub>	<0.03		4.5	2.2	4.0	3.6
Cr <sub>2</sub> O <sub>3</sub>	<0.05		0.74	0.40	0.73	0.57
FeO	8.9	0.16	5.8	5.6	5.8	5.7
MnO	0.13	0.05	0.19	0.13	0.14	0.14
MgO	50.3	0.17	32.9	35.2	33.5	34.1
CaO	0.03	0.02	0.75	0.43	0.62	0.70
Na <sub>2</sub> O	<0.03		<0.03	<0.03	<0.03	<0.03
K <sub>2</sub> O	<0.03		<0.03	<0.03	<0.03	<0.03
NiO	0.37	0.02	0.08	0.08	<0.08	0.14
total	100.9	0.3	100.1	101.6	100.5	101.4
X <sub>Mg</sub>	0.909	0.152	0.910	0.918	0.911	0.915
X <sub>Cr</sub>			0.100	0.107	0.108	0.095

Sample		M31				
Mineral	Olivine Average	STD (N = 8)	OPX-6-core	OPX-6-rim	OPX-3-core	OPX-3-core
SiO <sub>2</sub>	41.1	0.19	53.8	55.1	54.3	55.4
TiO <sub>2</sub>	<0.04		0.12	0.10	0.10	0.07
Al <sub>2</sub> O <sub>3</sub>	<0.03		5.7	4.6	5.1	3.8
Cr <sub>2</sub> O <sub>3</sub>	<0.05		0.70	0.50	0.52	0.30
FeO	9.6	0.14	6.1	6.4	5.9	6.3
MnO	0.14	0.03	0.12	0.19	0.19	0.13
MgO	49.7	0.22	32.5	32.8	32.5	33.4
CaO	0.03	0.02	0.64	0.67	0.76	0.63
Na <sub>2</sub> O	<0.03		0.07	0.06	<0.03	<0.03
K <sub>2</sub> O	<0.03		<0.03	<0.03	<0.03	<0.03
NiO	0.38	0.04	0.08	0.10	0.14	<0.08
total	101.1	0.4	99.9	100.5	99.5	100.1
X <sub>Mg</sub>	0.902	0.001	0.904	0.902	0.907	0.905
X <sub>Cr</sub>			0.076	0.068	0.064	0.050

STD = standard deviation, OPX = orthopyroxene, N = numbers of analyses, X<sub>Mg</sub> = Mg/(Mg + Fe<sup>total</sup>), X<sub>Cr</sub> = Cr/(Cr + Al).

**Table 2.** Representative spinel compositions.

Sample	M21		M31		M42DH	
	Average	STD (N = 7)	Average	STD (N = 15)	Average	STD (N = 5)
wt. %						
TiO <sub>2</sub>	0.05	0.03	<0.04		0.12	0.02
Al <sub>2</sub> O <sub>3</sub>	45.7	0.9	55.9	0.8	47.0	0.5
Cr <sub>2</sub> O <sub>3</sub>	21.9	1.3	11.6	0.7	20.2	0.6
Fe <sub>2</sub> O <sub>3</sub>	1.8	0.3	1.5	0.4	2.3	0.3
FeO	11.9	0.3	10.1	0.3	10.8	0.2
MnO	0.17	0.05	0.12	0.03	0.16	0.03
MgO	17.7	0.2	19.9	0.2	18.6	0.2
NiO	0.22	0.02	0.34	0.04	0.28	0.05
total	99.6	0.5	99.5	0.5	99.7	0.9
X <sub>Mg</sub>	0.726	0.007	0.778	0.006	0.753	0.006
X <sub>Cr</sub>	0.243	0.015	0.122	0.007	0.224	0.006
YFe <sup>3+</sup>	1.8	0.3	1.4	0.4	2.4	0.3
YAl	74.3	1.4	86.5	0.9	75.7	0.6
YCr	23.9	1.4	12.1	0.7	21.9	0.6

Fe<sub>2</sub>O<sub>3</sub> and FeO wt.% are calculated based on stoichiometry. STD = standard deviations, N = numbers of analyses, X<sub>Mg</sub> = Mg/(Mg + Fe<sup>2+</sup> for spinel, X<sub>Cr</sub> = Cr/(Cr + Al), YFe<sup>3+</sup> = Fe<sup>3+</sup>/(Fe<sup>3+</sup> + Al + Cr) for spinel, YAl = Al/(Fe<sup>3+</sup> + Al + Cr) for spinel, and YCr = Cr/(Fe<sup>3+</sup> + Al + Cr).

Table 3. Representative clinopyroxene compositions.

Sample		M31						
Occurrence	4-Core	4-Rim	10-fine	10-fine	11-fine	11-fine	12-fine	14-Core
wt.%								
SiO <sub>2</sub>	51.0	51.0	51.6	52.3	51.9	52.3	51.4	51.6
TiO <sub>2</sub>	0.25	0.24	0.37	0.35	0.31	0.34	0.3	0.32
Al <sub>2</sub> O <sub>3</sub>	6.9	5.1	5.6	5.6	6.2	5.3	6.5	6.9
Cr <sub>2</sub> O <sub>3</sub>	1.06	0.71	0.78	0.8	0.93	0.74	0.9	1.03
FeO	2.4	2.7	2.5	2.7	2.5	2.6	2.5	2.4
MnO	0.14	0.09	0.13	0.07	0.09	0.06	0.08	0.2
MgO	14.6	16.3	15.6	15.9	15.4	15.7	14.9	14.9
CaO	21.7	20.9	21.8	21.4	21.4	21.8	21.3	21.6
Na <sub>2</sub> O	0.95	0.7	0.92	0.88	1.01	0.86	1.07	1.05
K <sub>2</sub> O	<0.03	<0.03	<0.03	<0.03	<0.03	<0.03	<0.03	<0.03
NiO	<0.08	<0.08	<0.08	<0.08	<0.08	<0.08	<0.08	<0.08
Total	99.0	97.9	99.5	100.0	99.9	99.7	99.1	99.9
ppm								
Li	3.52	3.27	3.1	3.52	3.68	3.74	3.85	3.68
Ti	1802	2127	2105	2214	2004	2000	1946	1814
Sr	1.93	2	1.85	1.75	1.91	2.03	1.95	1.94
Y	12.23	12.76	12.07	12.66	11.77	11.26	11.7	11.74
Zr	3.31	4.04	4.15	4.04	3.61	3.54	3.56	3.21
Nb	0.12	0.1	0.1	0.1	0.1	0.09	0.12	0.11
La	<	<	<	<	<	<	<	<
Ce	0.16	0.17	0.14	0.16	0.16	0.15	0.16	0.16
Pr	0.09	0.10	0.08	0.08	0.09	0.08	0.10	0.09
Nd	1.04	1.03	0.94	0.97	1.04	0.95	1.07	1.05
Sm	0.72	0.77	0.72	0.76	0.79	0.70	0.84	0.70
Eu	0.35	0.36	0.34	0.35	0.36	0.35	0.36	0.34
Gd	1.39	1.42	1.34	1.41	1.39	1.30	1.44	1.35
Tb	0.28	0.32	0.25	0.27	0.28	0.25	0.26	0.25
Dy	2.12	2.23	2.10	2.20	2.10	2.00	2.12	2.05
Ho	0.47	0.50	0.47	0.49	0.45	0.44	0.46	0.45
Er	1.42	1.45	1.39	1.40	1.37	1.28	1.35	1.29
Tm	0.21	0.20	0.19	0.20	0.20	0.20	0.18	0.19
Yb	1.37	1.44	1.33	1.42	1.34	1.21	1.31	1.29
Lu	0.18	0.19	0.18	0.20	0.17	0.17	0.19	0.18
Hf	0.23	0.28	0.30	0.30	0.26	0.28	0.29	0.21
Sample		M21						
Occurrence	1	5-fine	7-Core	8-fine	8	13-fine	14-Core	
wt.%								
SiO <sub>2</sub>	52.3	52.2	52.1	52.2	52.0	52.5	52.2	
TiO <sub>2</sub>	0.2	0.22	0.12	0.18	0.19	0.19	0.17	
Al <sub>2</sub> O <sub>3</sub>	5.3	5.3	5.6	4.8	4.8	5.0	5.4	
Cr <sub>2</sub> O <sub>3</sub>	1.21	1.34	1.49	1.18	1.28	1.35	1.4	
FeO	2.2	2.4	2.4	2.3	2.0	2.3	2.5	
MnO	0.07	0.1	0.12	0.15	0.1	0.09	0.1	
MgO	15.5	15.6	15.5	16.2	15.9	15.7	15.5	
CaO	21.8	21.7	21.8	21.5	21.8	22.2	22.0	
Na <sub>2</sub> O	1	1.03	1.01	0.94	0.91	0.96	0.96	
K <sub>2</sub> O	<0.03	<0.03	<0.03	<0.03	<0.03	<0.03	<0.03	
NiO	<0.08	<0.08	<0.08	<0.08	<0.08	<0.08	<0.08	
Total	99.8	99.8	100.2	99.6	99.1	100.4	100.2	
ppm								
f Li	2.51	2.43	2.63	2.42	2.35	2.17	2.99	DL
Ti	972	1064	940	1008	972	1178	1012	0.51
Sr	3.08	3.08	2.95	2.63	2.73	2.53	2.46	0.01

Table 3. Cont.

Sample	M21								
	Occurrence	1	5-fine	7-Core	8-fine	8	13-fine	14-Core	
Y		6.17	7.37	6.53	6.35	6.53	6.8	6.44	0.01
Zr		1.87	2.06	1.75	1.72	1.72	1.92	1.65	0.02
Nb		0.18	0.17	0.19	0.14	0.16	0.18	0.15	0.01
La		<	<	<	<	<	<	<	0.01
Ce		0.18	0.17	0.16	0.14	0.14	0.14	0.14	0.01
Pr		0.06	0.06	0.06	0.05	0.05	0.05	0.05	0.01
Nd		0.50	0.55	0.49	0.41	0.45	0.47	0.45	0.03
Sm		0.35	0.39	0.34	0.29	0.32	0.31	0.31	0.05
Eu		0.17	0.19	0.17	0.18	0.16	0.17	0.17	0.02
Gd		0.65	0.75	0.67	0.66	0.69	0.76	0.66	0.03
Tb		0.13	0.16	0.14	0.15	0.14	0.14	0.14	0.01
Dy		1.05	1.26	1.16	1.08	1.11	1.15	1.05	0.03
Ho		0.24	0.28	0.26	0.23	0.24	0.26	0.25	0.01
Er		0.71	0.87	0.77	0.77	0.74	0.78	0.79	0.02
Tm		0.11	0.13	0.11	0.11	0.10	0.14	0.11	0.01
Yb		0.75	0.89	0.86	0.74	0.77	0.82	0.78	0.03
Lu		0.11	0.13	0.12	0.10	0.11	0.13	0.12	0.01
Hf		0.10	0.10	0.09	0.10	0.11	0.13	0.10	0.04

Data of trace element compositions are from [4]. DL = typical detection limit of analyses for 60  $\mu\text{m}$  laser diameter.

Table 4. Sr and Nd isotopic compositions of clinopyroxene from the lherzolite samples.

Sample#	$^{87}\text{Sr}/^{86}\text{Sr}$	2 sigma	$^{143}\text{Nd}/^{144}\text{Nd}$	2 sigma	Sm ppm	Nd ppm	$\epsilon\text{Nd}$ at Present	$\epsilon\text{Nd}$ at 100 Ma	$\epsilon\text{Nd}$ at 150 Ma
M21	0.702941	0.000017	0.513038	0.000043	0.4624	0.59938	7.8	4.4	2.6
M31	0.702817	0.000018	0.513303	0.000020	0.8373	1.1023	13.0	9.6	7.9

## 4. Results

### 4.1. Major and Trace Element Compositions of Minerals

The Fo ( $=100\text{Mg}/(\text{Mg} + \text{Fe})$  atomic ratio) and NiO content of olivine are 90 (M31)–91 (M21) and 0.4 wt.% (Figure 6), respectively. The  $X_{\text{Mg}}$  [ $=\text{Mg}/(\text{Mg} + \text{Fe}^{2+})$  atomic ratio], Cr# [ $=\text{Cr}/(\text{Cr} + \text{Al})$  atomic ratio] and  $Y_{\text{Fe}^{3+}}$  [ $100\text{Fe}^{3+}/(\text{Cr} + \text{Al} + \text{Fe}^{3+})$ ] of spinel are 0.79, 0.12 and 1.4 for M31, 0.73, 0.24 and 1.8 for M21, and 0.75, 0.22 and 2.4 for M42DH (dunite), respectively (Figure 7). The  $\text{TiO}_2$  content of spinel is usually lower than the detection limit of the analyses for lherzolites ( $<0.06$  wt.%), whereas that in the dunite (M42DH) is 0.12 wt.%. The  $X_{\text{Mg}}$  ( $=\text{Mg}/(\text{Mg} + \text{Fe}^{\text{total}})$  atomic ratio) of orthopyroxene increases from M31 (0.90) to M21 (0.91). The  $\text{Al}_2\text{O}_3$  content of orthopyroxene usually decreases from core to rim in both lherzolites. The  $\text{Al}_2\text{O}_3$  content of orthopyroxene cores is 5.7 wt.% in M31 and 4.5 wt.% in M21 (Figure 8). The  $\text{TiO}_2$  content of orthopyroxene is usually low ( $<0.1$  wt.%). Clinopyroxenes are high in  $\text{Al}_2\text{O}_3$  contents, up to 5.6 wt.% and 6.9 wt.% for M21 and M31, respectively. The  $\text{Na}_2\text{O}$  and  $\text{TiO}_2$  contents of clinopyroxene are 1 wt.% and 0.1–0.3 wt.%, respectively. Chondrite-normalized REE patterns of clinopyroxene are depleted in light rare earth elements (LREE) and fluid-mobile elements (Figure 9).

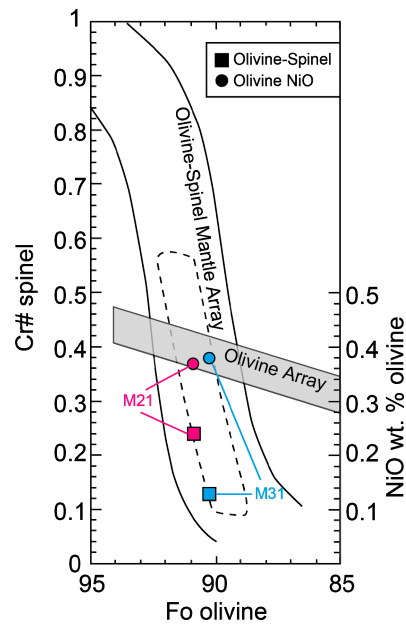


**Figure 6.** Compositional relationships between the Fo and NiO contents of olivine, and the Fo content of olivine and the Cr# of coexisting spinel. Mantle Olivine Array (Olivine Array in the diagram) is from [21]. Olivine-Spinel Mantle Array shows the compositional range for residual peridotites in spinel peridotites [22,23]. Compositional ranges of the OSMA for the Middle-North Andaman peridotites [11] are also shown in a dashed line.

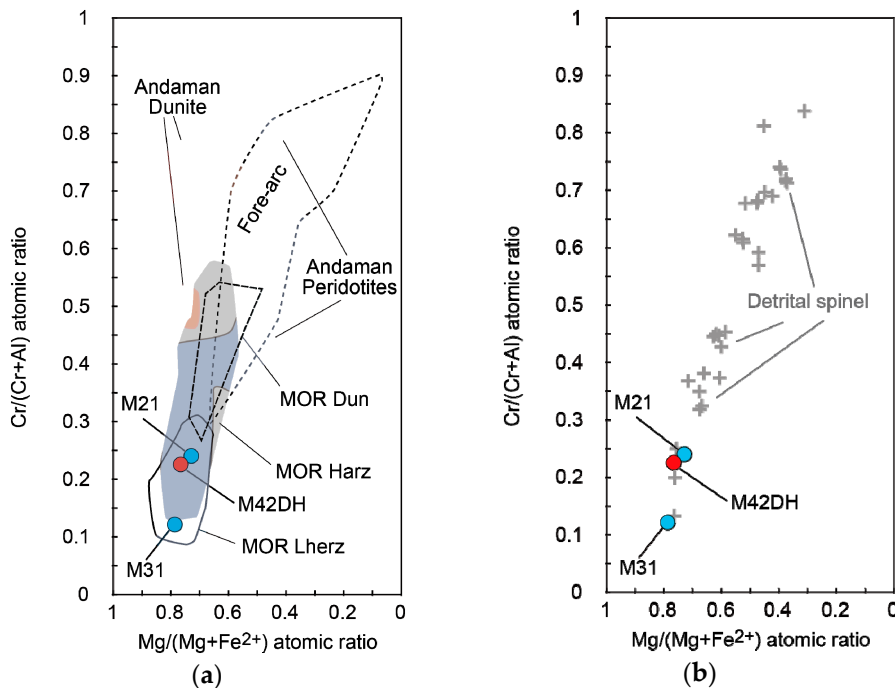


**Figure 7.** Relationship between the Mg# and Cr# of spinel. (a) Chemical comparison between the studied samples vs the compositional ranges for mid-ocean ridge lherzolite (MOR Lherz: solid line), harzburgite (MOR Harz: dark) and dunite (MOR Dun: broken line) [24], for forearc peridotites (broken line) compiled by [7] and for the Andaman dunites (pinkish) and Peridotites (light blue) are from [9]. (b) Chemical comparison between the studied sample and detrital chromian spinels from the Middle Andaman Island [11].

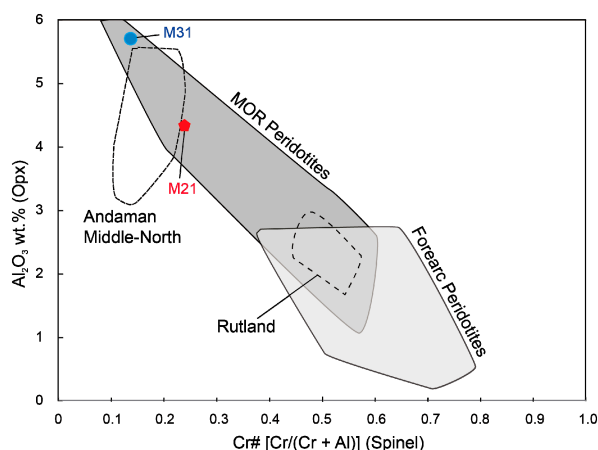


**Figure 8.** Relationship between the  $\text{Al}_2\text{O}_3$  contents of orthopyroxene porphyroclast core and the Cr# of spinel. The compositional ranges for mid-ocean ridge peridotites (MOR Peridotites) and Forearc peridotites are compiled by [25], and for the Andaman ophiolites are from [9].

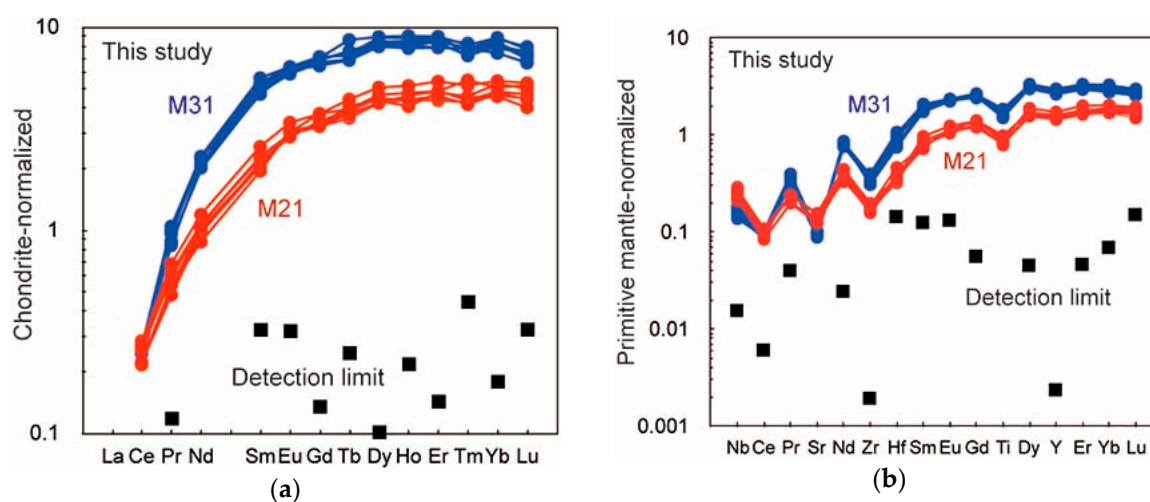


**Figure 9.** (a) Chondrite-normalized REE patterns and (b) primitive-mantle-normalized trace element patterns of the M21 (Red) and M31 (Blue) lherzolite clinopyroxenes. Data are from [4]. The typical detection limit of elemental analyses is also shown for 60  $\mu\text{m}$  that was used for obtaining trace element compositions of clinopyroxenes. Chondrite and primitive mantle values are from [26].

#### 4.2. Sr and Nd Isotopic Compositions of Clinopyroxene

Figure 7 shows the variation in the relationships between  $^{143}\text{Nd}/^{144}\text{Nd}$  and  $^{87}\text{Sr}/^{86}\text{Sr}$  for clinopyroxenes. Clinopyroxenes from abyssal peridotites recovered from the Southwest Indian Ridge (SWIR) is also plotted in Figure 7. High Sr-isotopic compositions in the SWIR abyssal peridotites are interpreted as the Sr contributions due to seawater alteration [27]. According to Sr-isotopic compositions, the effect of seawater contamination appears to be least in the selected samples. The sample M21 ( $^{143}\text{Nd}/^{144}\text{Nd} = 0.513038$ ) is relatively more enriched than the depleted MORB mantle (DMM), whereas the M31 ( $^{143}\text{Nd}/^{144}\text{Nd} = 0.513303$ ) is more depleted than the DMM. In the Sr-Nd isotopic systematics the plots for these spinel lherzolites extend to the peridotite field recovered from the SWIR. There is no visible evidence for enriched isotopic compositions in these samples.

We have calculated  $\epsilon\text{Nd}$  isotopic composition from the present to 100–150 Ma using the measured  $^{147}\text{Sm}/^{144}\text{Nd}$  data (Figure 8, Table 4). Because of very low Rb/Sr ratios in residual clinopyroxenes, age correction has not been considered for the Sr isotopic compositions.

## 5. Discussion

### 5.1. Petrogenesis of Lherzolites in the Mantle Section of the Middle Andaman Ophiolite

The mantle section of the Andaman ophiolite is characterized by variable depletion in melt components and consists of a broad spectrum of peridotites ranging from harzburgite (Rutland Island) to lherzolite (middle/north Islands) [12]. Fresh rock exposures are limited in the eastern part of the Andaman Islands, which covers our study area. Ghosh et al. [11] examined the chemical variations of the least altered detrital spinel to understand the general characteristics of the Andaman Ophiolite. Detrital spinel compositions of the Middle Andaman cover a wide range of variations (Figure 7b). The spinel heterogeneity with their low  $\text{TiO}_2$  wt.% and  $\text{Fe}^{3+}/(\text{Cr} + \text{Al} + \text{Fe}^{3+})$  ratio [11] could be attributed to the large variation in the degree of partial melting. The studied lherzolites are plotted at high-Cr# (M21) and low-Cr# (M31) ends of the chemical range for the lherzolitic samples of abyssal peridotites recovered from the the mid-ocean ridges (Figure 9).

As a first-order consideration for the Middle Andaman lherzolites, low-Cr# in spinels (Figures 6–8) together with slight depletion in LREEs in the coexisting clinopyroxenes (Figure 9) suggest a residual origin formed after low-degree of partial melting.

Spinel chemistry and clinopyroxene HREEs contents indicate that M21 has likely suffered a slightly higher degree of melting than M31 (Figure 9). However, highly incompatible elements, such as LREEs and Sr, are not much depleted in M21 than that expected from fractional melting (Figure 6). It is also noted that the degree of melting undergone by the Middle Andaman lherzolites correlates inversely with their  $^{143}\text{Nd}/^{144}\text{Nd}$  ratios (Figure 10). Similar inverse correlations have also been documented from the Mid-Atlantic Ridge [28] and also from the Southwest Indian Ridge [27]. The inverse relationships between the degree of partial melting and  $^{143}\text{Nd}/^{144}\text{Nd}$  ratios can be explained by the interaction between depleted peridotite and a migrating isotopically enriched melt [27,28].

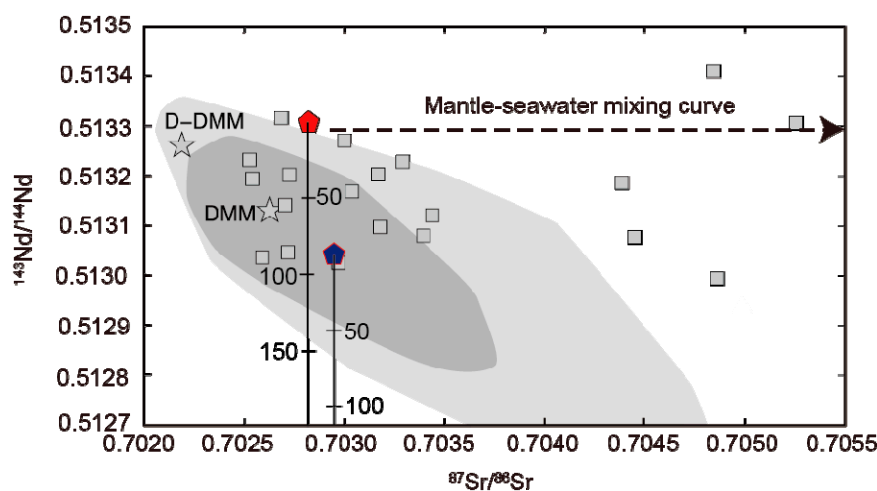


**Figure 10.**  $^{143}\text{Nd}/^{144}\text{Nd}$ - $^{87}\text{Sr}/^{86}\text{Sr}$  isotopic compositions of clinopyroxene in the Middle Andaman lherzolites. The compositional ranges for mid-ocean ridge basalts (MORB) and peridotites (light grey square) are from [27]. The dark grey area (MORB\*) is a compositional range with a higher density among the MORB data. The DMM and D-DMM values are from [29,30], respectively. Mantle-seawater mixing curve (broken arrow) is referred from [28].

We initially compared residues after fractional melting from depleted MORB mantle (DMM) [30] at spinel peridotite stability pressure-temperature conditions. Melting stoichiometries are 1 melt = 0.05 spinel + 0.45 orthopyroxene + 0.75 clinopyroxene – 0.25 olivine (simplified after [31]). Trace element pattern of M31 clinopyroxene is consistent with a residue after 2–5% fractional melting (the first-stage melting) (Figure 11a). Then we assumed that a residue resulted from fractional melting of DMM (the first stage melting), such as M31, reacted with an accumulated melt also generated during

the first stage fractional melting. We modeled the clinopyroxene trace element patterns using an open-system melting model, in which the input and output of fluids/melts are associated with partial melting and melt extraction of the peridotite itself [32,33]. We considered the starting composition and the influx compositions as a residue following 2.5% fractional melting of DMM under spinel peridotite conditions; and their accumulated melt, respectively. Additional 2.5–10% melting was also used for the second stage melting (flux-induced open-system melting). Melting proportions for the open system melting are the same as the fractional melting model. We used reasonable parameters for open-system melting: (1) the presence of a critical melt fraction in the system, at which the system becomes open to melt separation at a constant rate of  $\alpha = 0.02$ , and (2) a dimensionless influx rate (influxed mass fraction of the initial solid, divided by the degree of melting) of  $\beta = 0.25$ . The effect of trapped melt crystallization was not considered. Trace element patterns of the M21 clinopyroxene, higher degree of partial melting coupled with higher LREE/HREE ratio than the M31, are quantitatively reproduced by this model (Figure 11b).

It is concluded that the major and trace element characteristics of the studied lherzolite samples can be explained by partial melting from the DMM and interaction with their melts. The tectonic setting for these melting and melt-rock interactions is suitable for mid-ocean ridge and/or back-arc where adiabatic partial melting and melt migration are expected. Although we cannot constrain the melting age of the studied samples, the minimum age is constrained by zircon dating  $>95$  Ma from plagiogranite [14–17]. The age-corrected  $\epsilon\text{Nd}$  isotopic compositions for the 100 Ma to 200 Ma M31 are 9.6–6.3 (Figure 7), and are in consistent with the MORB-type mantle source.

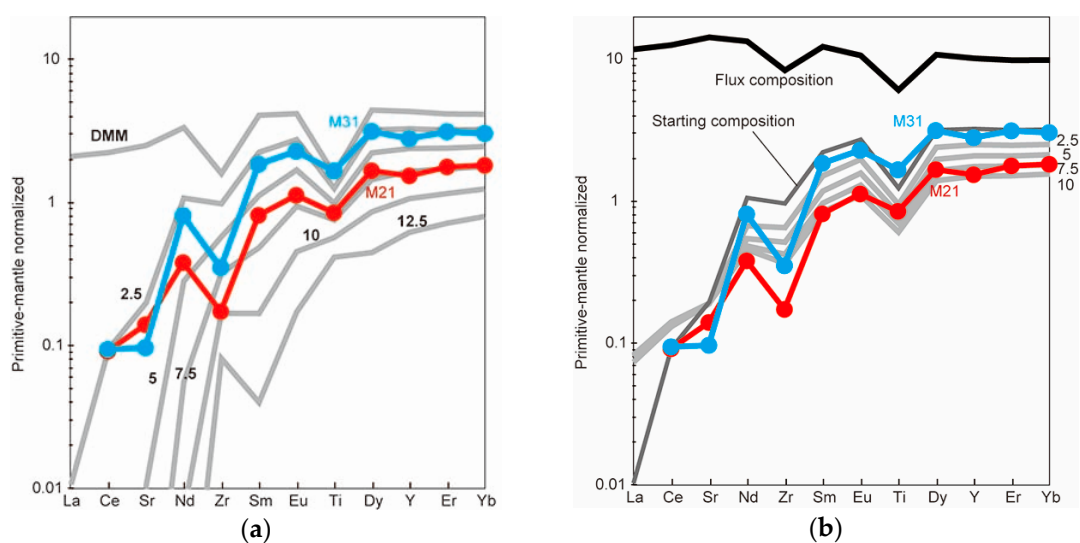


**Figure 11.** Averaged and modeled primitive-mantle-normalized trace element patterns for clinopyroxenes. Details of how the data were obtained are outlined in the text. (a) Modeled clinopyroxene trace element compositions after fractional melting under the spinel peridotite stability field. The 2.5, 5, 7.5, 10 and 12.5 degrees of partial melting after fractional melting are shown. (b) Modeled clinopyroxene compositions after influx melting under conditions of the spinel peridotite stability field. The influx composition is the accumulated melt after 2.5% fractional melting modeled in (a). The 2.5, 5, 7.5, and 10 degrees of partial melting after influx-induced open-system melting are also shown. Mineral/melt partition coefficients are from [31,33]. Melting models were obtained using the spreadsheet of [33].

## 5.2. Dunite Petrogenesis and Its Implication for Tectonic Evolution

The boundary between the studied dunite and its host peridotite is very sharp. The Cr# of spinel (0.22) in the studied dunite is not high enough to be a residue after high-degree of partial melting. These characteristics suggest that the dunite was formed by melt-rock reaction [34,35]. Spinel composition

in the dunite is within the chemical range of mid-ocean ridge dunite [24,36,37], whereas spinels in chromitites from the North Andaman region has two populations: high- and intermediate-Cr# [4]. The high Cr# chromitites are interpreted to be formed by interaction with arc-related magmas. The distinctive characteristics of spinel compositions of the dunite and chromitites in the Middle-North Andaman mantle section suggest involvement of at least two distinctive melts, at least, in the formation of the Andaman ophiolite: (1) mid-ocean ridge-like melt for the low-intermediate Cr# dunites/chromitites and (2) arc-related magmas for high-Cr# dunites/chromitites.

In summary, it is concluded that although the Andaman Ophiolite is modified by arc-related magmatism later in its history, the studied peridotites in the Middle Andaman are least affected by this process and represent a window to explore the upper mantle materials below the southeastern end of the Tethyan ocean.

### 5.3. Comparison with Other Tethyan Ophiolites

Both spinel lherzolite and plagioclase peridotite are observed in the western Tethyan ophiolites e.g., [38] and references therein. Trace element compositions of clinopyroxenes in these spinel peridotites can be divided into two types: (1) moderately depleted trace element pattern with a weak LREE to HREE fractionation (e.g., External Liguride [39]), and (2) significant fractionation of LREE to HREE (e.g., Internal Liguride; [40]). The lherzolites in this study are almost identical to the latter one (Figure 9).

We compiled  $\epsilon\text{Nd}$  isotopic data of clinopyroxene of spinel lherzolites with LREE-depleted patterns from the western Tethyan ophiolites [39–42] (Figure 9). Although the melting age for the Middle Andaman Ophiolite has not been well constrained yet, it is presumed to be older than 100 Ma of the plagiogranite intrusion ages [14–17]. The estimated initial  $\epsilon\text{Nd}$  values of the Tethyan lherzolite clinopyroxenes with LREE-depleted patterns are likely to be consistent with the depleted mantle evolution line (Figure 12).

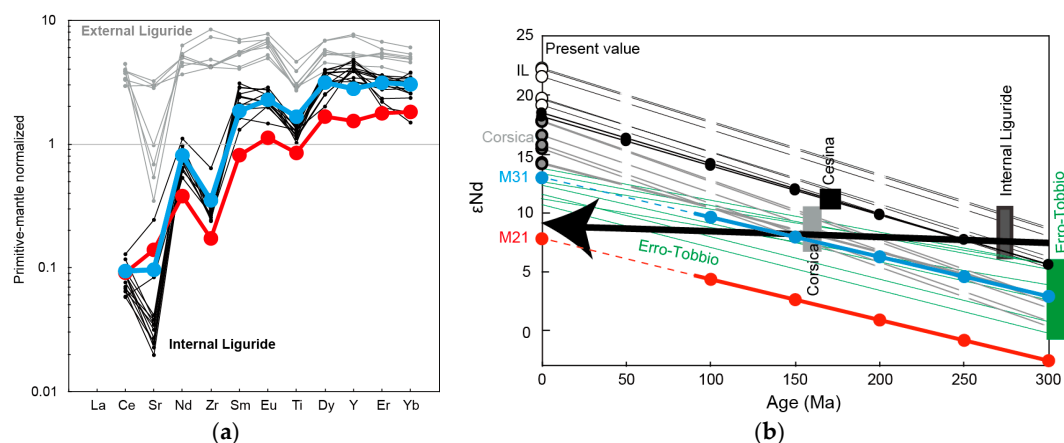


**Figure 12.** (a) Primitive-mantle-normalized trace element patterns of averaged clinopyroxene from the Middle Andaman and those of clinopyroxenes in spinel lherzolites from the Internal Liguride and External Liguride peridotites [39,40]. (b) Relationships between  $\epsilon\text{Nd}$  of clinopyroxene and time for the studied Middle Andaman Ophiolite and the western Tethyan ophiolites. The  $\epsilon\text{Nd}$  values at 275 Ma for Internal Liguride [40], at 160 Ma for Corsica [41], and at 175 Ma for Cesina [42] are interpreted as initial  $\epsilon\text{Nd}$  values. The  $\epsilon\text{Nd}$  value of the Erro-Tobbio at 300 Ma is the value at the time of emplacement of the massif [43]. Depleted mantle evolution model (large arrow) is from [44].

## 6. Conclusions

We examined two lherzolites and associated dunite from the Middle Island of the Andaman Ophiolite. Field occurrence and mineral chemistry of these samples indicate their origin as residue after partial melting from the DMM compositions for the lherzolites and a reaction product with MORB-like melt for the dunite. Although the melting ages for the studied samples have not been well constrained yet, the  $\epsilon\text{Nd}$  of clinopyroxene of the lherzolite samples are consistent with MORB-type mantle source. Clinopyroxene in the studied Andaman lherzolites are depleted in LREEs and are similar to those from the western Tethyan ophiolites. The  $\epsilon\text{Nd}$  isotopic data of the Tethyan lherzolite clinopyroxenes with LREE-depleted patterns are likely to be consistent with the depleted mantle evolution line.

**Author Contributions:** T.M. and B.G. did field survey and major element analyses of minerals. T.M., J.M.G. and B.G. prepared the manuscript. M.Y. separated clinopyroxenes from the samples and analyzed their Sr and Nd isotopic compositions. A.T. analyzed trace element compositions of minerals.

**Funding:** This study was financially supported by a Grant-in-Aid for Scientific Research of the Ministry of Education Culture, Sports, Science and Technology of Japan (No. 21403010), Special Coordination Funds for Promoting Science and Technology (SCF) to Improve Research Environments for Young Researchers, and Researcher Exchange Program between Japan Society for the Promotion of Science (JSPS) and Indian National Science Academy (INSA) to TM and a JSPS Invitation Fellowship to BG.

**Acknowledgments:** We are grateful to S. Umino and T. Mizukami for discussions. T.M. would like to thank K. Ozawa for providing the spread sheet of Ozawa (2001). Arai kindly gave us an opportunity for contributing to this special volume on mantle petrology. Comments from three anonymous reviews significantly improved the manuscript.

**Conflicts of Interest:** The authors declare no conflict of interest. The founding sponsors had no role in the design of the study; in the collection, analyses, or interpretation of data; in the writing of the manuscript, and in the decision to publish the results.

## References

- Dilek, Y.; Furnes, H. Ophiolite genesis and global tectonics: Geochemical and tectonic fingerprinting of ancient oceanic Lithosphere. *Geol. Soc. Am. Bull.* **2011**, *123*, 387–411. [[CrossRef](#)]
- Metcalf, I. Gondwana dispersion and Asian accretion: Tectonic and palaeogeographic evolution of eastern Tethys. *J. Asian Earth Sci.* **2013**, *66*, 1–33. [[CrossRef](#)]
- Liu, C.-Z.; Zhan, C.; Xu, Y.; Wang, J.-G.; Chen, Y.; Guo, S.; Wu, F.-Y.; Sein, K. Petrology and geochemistry of mantle peridotites from the Kalaymyo and Myitkyina ophiolites (Myanmar): Implications for tectonic settings. *Lithos* **2016**, *264*, 495–508. [[CrossRef](#)]
- Ghosh, B.; Mukhopadhyay, S.; Morishita, T.; Tamura, A.; Arai, S.; Bandyopadhyay, D.; Chattopadhyaya, S.; Ovung, T.N. Diversity and evolution of suboceanic mantle: Constraints from Neotethyan ophiolites at the eastern margin of the Indian plate. *J. Asian Earth Sci.* **2018**, *160*, 67–77. [[CrossRef](#)]
- Boudier, F.; Nicolas, A. Harzburgite and lherzolite subtypes in ophiolitic and oceanic environments. *Earth Planet. Sci. Lett.* **1985**, *76*, 84–92. [[CrossRef](#)]
- Picazo, S.; Müntener, O.; Manatschal, G.; Bauville, A.; Karner, G.; Johnson, C. Mapping the nature of mantle domains in Western and Central Europe based on clinopyroxene and spinel chemistry: Evidence for mantle modification during an extensional cycle. *Lithos* **2016**, *266–267*, 233–263. [[CrossRef](#)]
- Morishita, T.; Dilek, Y.; Shallo, M.; Tamura, A.; Arai, S. Insight into the uppermost mantle section of a maturing arc: The Eastern Mirdita ophiolite, Albania. *Lithos* **2011**, *124*, 215–226. [[CrossRef](#)]
- Ghosh, B.; Pal, T.; Bhattacharya, A.; Das, D. Petrogenetic implications of ophiolitic chromite from Rutland Island, Andaman—a boninitic parentage in supra-subduction setting. *Mineral. Petrol.* **2009**, *96*, 59–70. [[CrossRef](#)]
- Ghosh, B.; Morishita, T.; Bhatta, K. Significance of chromian spinels from the mantle sequence of the Andaman Ophiolite, India: Paleogeodynamic implications. *Lithos* **2013**, *164–167*, 86–96. [[CrossRef](#)]
- Pal, T. Petrology and geochemistry of the Andaman ophiolite: Melt-rock interaction in a suprasubduction-zone setting. *J. Geol. Soc. Lond.* **2011**, *168*, 1031–1045. [[CrossRef](#)]

11. Ghosh, B.; Morishita, T.; Bhatta, K. Detrital chromian spinels from beach placers of Andaman Islands, India: A perspective view of petrological characteristics and variations of the Andaman ophiolite. *Isl. ARC* **2012**, *21*, 188–201. [CrossRef]
12. Ghosh, B.; Bandyopadhyay, D.; Morishita, T. Andaman–Nicobar Ophiolites, India: Origin, evolution and emplacement. *Geol. Soc. Lond. Mem.* **2017**, *47*, 95–110. [CrossRef]
13. Curray, J.R. Tectonics and history of the Andaman Sea region. *J. Asian Earth Sci.* **2005**, *25*, 187–228. [CrossRef]
14. Pedersen, R.B.; Searle, M.P.; Carter, A.; Bandyopadhyay, P.C. U–Pb zircon age of the Andaman ophiolite: Implications for the beginning of subduction beneath the Andaman–Sumatra arc. *J. Geol. Soc. Lond.* **2010**, *167*, 1105–1112. [CrossRef]
15. Sarma, D.S.; Jafri, S.H.; Fletcher, I.R.; McNaughton, N.J. Constraints on the tectonic setting of the Andaman ophiolites, Bay of Bengal, India, from SHRIMP U–Pb zircon geochronology of plagiogranite. *J. Geol.* **2010**, *118*, 691–697. [CrossRef]
16. Singh, A.K.; Chung, S.-L.; Bikramaditya, R.K.; Lee, H.Y. New U–Pb zircon ages of plagiogranites from the Nagaland–Manipur Ophiolites, Indo–Myanmar Orogenic Belt, NE India. *J. Geol. Soc. Lond.* **2016**, *174*, 170–191. [CrossRef]
17. Jafri, S.H.; Charan, S.N.; Govil, P.K. Plagiogranite from the Andaman ophiolite belt, Bay of Bengal, India. *J. Geol. Soc. Lond.* **1995**, *152*, 681–687. [CrossRef]
18. Snow, J.E.; Hart, S.R.; Dick, H.J.B. Orphan Sr-87 in abyssal peridotites—Daddy was a granite. *Science* **1993**, *262*, 1861–1863. [CrossRef] [PubMed]
19. Yoshikawa, M.; Nakamura, E.; Takahashi, E. Rb–Sr isotope systematics in a phlogopite-bearing spinel lherzolite and its implications for age and origin of metasomatism in the Horoman peridotite complex, Hokkaido, Japan. *J. Min. Petrol. Econ. Geol.* **1993**, *88*, 121–130. [CrossRef]
20. Shibata, T.; Yoshikawa, M. Precise isotope determination of trace amounts of Nd in ultramafic rock samples. *J. Mass Spec. Soc. Jpn.* **2004**, *52*, 317–324. [CrossRef]
21. Takahashi, E.; Uto, K.; Schilling, J.G. Primary Magma Compositions and Mg/Fe Ratios of their Mantle Residues along Mid Atlantic Ridges 29° N to 73° N. In *Technical Report of ISEI*; Okayama University: Okayama, Japan, 1987; Volume A-9; pp. 1–12.
22. Arai, S. An estimation of the least depleted spinel peridotite on the basis of olivine-spinel mantle array. *Neues Jahrb. Mineral.-Mon.* **1987**, *8*, 347–354.
23. Arai, S. Characterization of spinel peridotites by olivine-spinel compositional relationships: Review and interpretation. *Chem. Geol.* **1994**, *113*, 191–204. [CrossRef]
24. Warren, J.M. Global variations in abyssal peridotite compositions. *Lithos* **2016**, *248–251*, 193–219. [CrossRef]
25. Morishita, T.; Nakamura, K.; Shibuya, T.; Kumagai, H.; Sato, T.; Okino, K.; Sato, H.; Nauchi, R.; Hara, K.; Takamaru, R. Petrology of peridotites and related gabbroic rocks around the Kairei Hydrothermal Field in the Central Indian Ridge. In *Subseafloor Biosphere Linked to Hydrothermal Systems: TAIGA Concept*; Ishibashi, J.-I., Ed.; Springer: Tokyo Heidelberg New York Dordrecht London, 2015; Available online: [https://link.springer.com/chapter/10.1007/978-4-431-54865-2\\_14](https://link.springer.com/chapter/10.1007/978-4-431-54865-2_14) (accessed on 17 September 2018).
26. McDonough, W.F.; Sun, S.-S. The composition of the Earth. *Chem. Geol.* **1995**, *120*, 223–253. [CrossRef]
27. Warren, J.M.; Shimizu, N.; Sakaguchi, C.; Dick, H.J.B.; Nakamura, E. An assessment of upper mantle heterogeneity based on abyssal peridotite isotopic compositions. *J. Geophys. Res.* **2009**, *114*, B12203. [CrossRef]
28. Cipriani, A.; Brueckener, H.K.; Bonatti, E.; Brunelli, D. Oceanic crust generated by elusive parents: Sr and Nd isotopes in basalt-peridotite pairs from the Mid-Atlantic Ridge. *Geology* **2004**, *32*, 657–660. [CrossRef]
29. Su, Y.; Langmuir, C.H. Global MORB Chemistry Compilation at the Segment Scale. Ph.D. Thesis, Department of Earth and Environmental Science, Columbia University, New York, NY, USA, 2003.
30. Workman, R.K.; Hart, S.R. Major and trace element compositions of the depleted MORB mantle (DMM). *Earth Planet. Sci. Lett.* **2005**, *231*, 53–72. [CrossRef]
31. Kinzler, R.J.; Grove, T.L. Primary magmas of mid-ocean ridge basalts 1. Experiments and Methods. *J. Geophys. Res.* **1992**, *97*, 6885–6906. [CrossRef]
32. Ozawa, K. Mass balance equations for open magmatic systems: Trace element behavior and its application to open system melting in the upper mantle. *J. Geophys. Res.* **2001**, *106*, 13407–13434. [CrossRef]
33. Ozawa, K.; Shimizu, N. Open-system melting in the upper mantle: Constraints from the Hayachine–Miyamori ophiolite, northeastern Japan. *J. Geophys. Res.* **1995**, *100*, 22315–22335. [CrossRef]

34. Kelemen, P.B. Reaction between ultramafic rocks and fractionating basaltic magma I. Phase relations, the origin of calc-alkaline magma series, and the formation of discordant dunite. *J. Petrol.* **1990**, *31*, 51–98. [[CrossRef](#)]
35. Kelemen, P.B.; Shimizu, N.; Salters, V.J.M. Extraction of mid-ocean-ridge basalt from the upwelling mantle by focused flow of melt in dunite channels. *Nature* **1995**, *375*, 747–753. [[CrossRef](#)]
36. Morishita, T.; Maeda, J.; Miyashita, S.; Kumagai, H.; Matsumoto, T.; Dick, H.J.B. Petrology of local concentrate of Chromian spinel in dunite from the slow-spreading Southwest Indian Ridge. *Eur. J. Mineral.* **2007**, *19*, 871–882. [[CrossRef](#)]
37. Payot, B.D.; Arai, S.; Dick, H.J.B.; Abe, N.; Ichiyama, Y. Podiform chromitite formation in a low-Cr/high-Al system: An example from the Southwest Indian Ridge (SWIR). *Mineral. Petrol.* **2014**, *108*, 533–549. [[CrossRef](#)]
38. Müntener, O.; Pettke, T.; Desmurs, L.; Meier, M.; Schaltegger, U. Refertilization of mantle peridotite in embryonic ocean basins: Trace element and Nd isotopic evidence and implications for crust-mantle relationships. *Earth Planet. Sci. Lett.* **2004**, *221*, 293–308. [[CrossRef](#)]
39. Rampone, E.; Hofmann, A.W.; Piccardo, G.B.; Vannucci, R.; Bottazzi, P.; Ottolini, L. Petrology, mineral and isotope geochemistry of the External Liguride Peridotites (Northern Apennines, Italy). *J. Petrol.* **1995**, *36*, 81–105. [[CrossRef](#)]
40. Rampone, E.; Hofmann, A.W.; Piccardo, G.B.; Vannucci, R.; Bottazzi, P.; Ottolini, L. Trace element and isotope geochemistry of depleted peridotites from an N-MORB type ophiolite (Internal Liguride, N. Italy). *Contrib. Mineral. Petrol.* **1996**, *123*, 61–76. [[CrossRef](#)]
41. Rampone, E.; Hofmann, A.W.; Raczek, I. Isotopic equilibrium between mantle peridotite and melt: Evidence from the Corsica ophiolite. *Earth Planet. Sci. Lett.* **2009**, *288*, 601–610. [[CrossRef](#)]
42. Tribuzio, R.; Thirlwall, M.F.; Vannucci, R. Origin of gabbro-peridotite association from the Northern Apennine Ophiolites (Italy). *J. Petrol.* **2004**, *45*, 1109–1124. [[CrossRef](#)]
43. Rampone, E.; Romairone, A.; Abouchami, W.; Piccardo, G.B.; Hofmann, A.W. Chronology, petrology and isotope geochemistry of the Erro-Tobbio peridotites (Ligurian Alps, Italy): Records of late Palaeozoic lithospheric extension. *J. Petrol.* **2005**, *46*, 799–827. [[CrossRef](#)]
44. DePaolo, D.J. Neodymium isotopes in the Colorado Front Range and crust-mantle evolution in the Proterozoic. *Nature* **1981**, *291*, 193–196. [[CrossRef](#)]



© 2018 by the authors. Licensee MDPI, Basel, Switzerland. This article is an open access article distributed under the terms and conditions of the Creative Commons Attribution (CC BY) license (<http://creativecommons.org/licenses/by/4.0/>).